SOFT ROBOTICS
Volume 00, Number 00, 2017
© Mary Ann Liebert, Inc.
DOI: 10.1089/soro.2017.0002

SoRo
Soft Robotics

ORIGINAL ARTICLE

Downloaded by Harvard University FRANCIS A COUNTWAY from online.liebertpub.com at 10/17/17. For personal use only.

A Biologically Inspired, Functionally Graded End Effector for Soft Robotics Applications

Kitty Kumar,[1,*] Jia Liu,[2,*] Caleb Christianson,[3] Mustafa Ali,[4] Michael T. Tolley,[4] Joanna Aizenberg,[1,2] Donald E. Ingber,[1,2,5] James C. Weaver,[1] and Katia Bertoldi[2]

Abstract

Soft robotic actuators offer many advantages over their rigid counterparts, but they often are unable to apply highly localized point loads. In contrast, many invertebrates have not only evolved extremely strong ''hybrid appendages'' that are composed of rigid ends that can grasp, puncture, and anchor into solid substrates, but they also are compliant and resilient, owing to the functionally graded architecture that integrates rigid termini with their flexible and highly extensible soft musculatures. Inspired by the design principles of these natural hybrid appendages, we demonstrate a synthetic hybrid end effector for soft-bodied robots that exhibits excellent piercing abilities. Through the incorporation of functionally graded interfaces, this design strategy minimizes stress concentrations at the junctions adjoining the fully rigid and soft components and optimizes the bending stiffness to effectively penetrate objects without interfacial failure under shear and compressive loading regimes. In this composite architecture, the radially aligned tooth-like elements apply balanced loads to maximize puncturing ability, resulting in the coordinated fracture of an object of interest.

Keywords: bioinspired robotics, multi-material 3D printing, hybrid end effectors

Introduction

Hybrid, functionally graded end effectors offer great potential for soft robotic systems[1–6] because they can apply highly localized stresses by using rigid components for puncturing and anchoring into solid substrates, while taking advantage of the damage tolerance and compliant nature of the underlying soft actuators.[7–11] It is a major challenge, however, to design and structurally optimize these hybrid end effectors for high strength and functionality under a diverse range of loading conditions. In contrast to their engineering counterparts, however, many biological systems seamlessly integrate rigid tooth-like structures into soft flexible tissues to achieve effective grasping, puncturing, and anchoring abilities.[12] Examples include the mineralized jaws of predatory marine worms,[13] the hooked anchoring apparatus of tapeworms,[14] and the robust sucker ring teeth found in the arms and tentacles of squid and cuttlefish.[15] These biological piercing and anchoring appendages primarily follow two design strategies to sustain high stress under complex loading conditions: (1) Multiple sharp tooth-like structures are radially arranged within the appendage and actuated via the contraction of the surrounding musculature to apply balanced localized forces from multiple directions and ensure an excellent stability during puncturing (Fig. 1A), and (2) each tooth within the appendage incorporates a functionally graded architecture (Fig. 1B), which facilitates effective piercing, while simultaneously accommodating lateral bending of the teeth during loading. For example, in *Glycera* jaws, the graded mechanical properties are a direct consequence of the extent of mineralization within the jaws,[13] whereas in the squid sucker ring teeth, the modulus gradient is driven by the variability in pore fraction within the tooth structure.[15]

[1]Wyss Institute for Biologically Inspired Engineering, Harvard University, Boston, Massachusetts.
[2]Harvard John A. Paulson School of Engineering and Applied Sciences, Harvard University, Cambridge, Massachusetts.
[3]Department of NanoEngineering, University of California, San Diego, California.
[4]Department of Mechanical and Aerospace Engineering, University of California, San Diego, California.
[5]Vascular Biology Program, Boston Children's Hospital and Harvard Medical School, Boston, Massachusetts.
*Co-first authors.

Downloaded by Harvard University FRANCIS A COUNTWAY from online.liebertpub.com at 10/17/17. For personal use only.

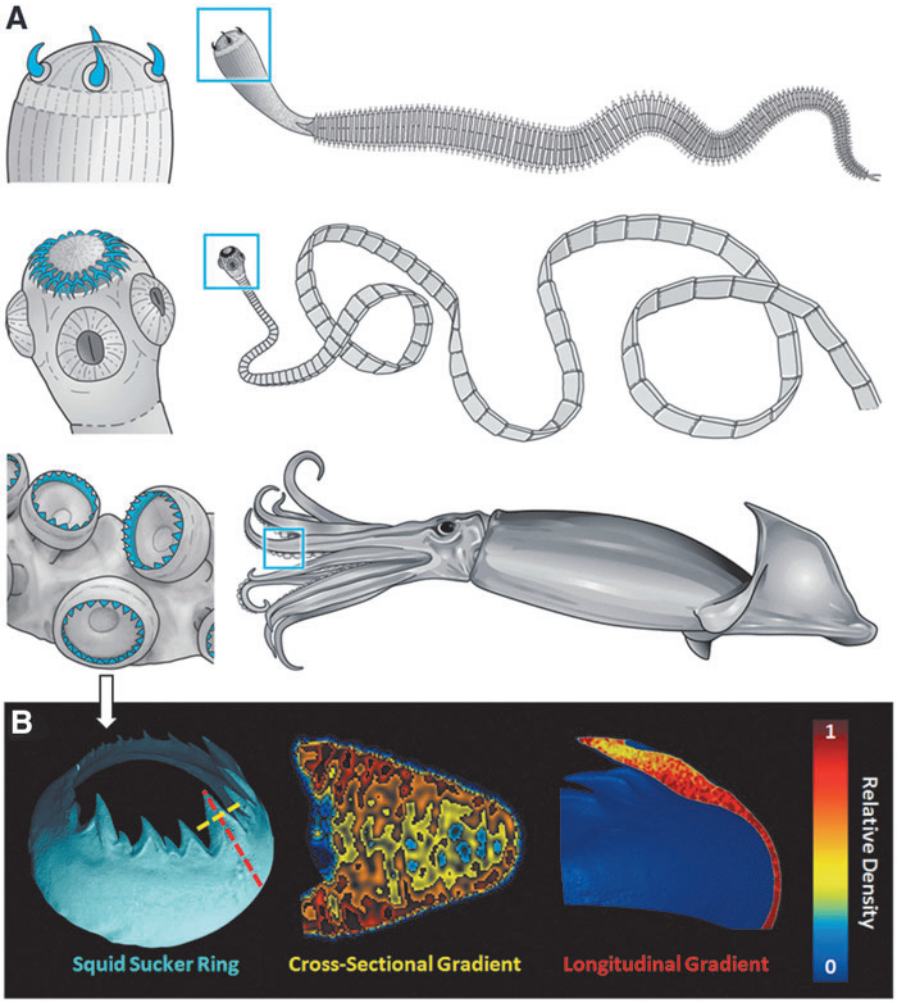

FIG. 1. **(A)** Examples of radially organized puncturing and anchoring structures found in nature include the mineralized jaws of the marine bloodworms (*top*), the anchoring hooks of the tapeworm scolex (*center*), and the abrasion-resistant sucker ring teeth found in squid arms and tentacles (*bottom*). In each example, the cutting or anchoring jaws, hooks, and teeth are highlighted in *blue*. **(B)** Cross-sectional (*yellow dotted line*) and longitudinal (*red dotted line*) virtual tomographic sections through an isolated squid sucker ring clearly illustrate the multi-directional modulus gradients (reflected in electron density profiles) in both directions. The density profile is the result of varying pore fraction that results in the modulus gradient within the structure.

Although these biological systems offer excellent inspiration for the design of synthetic hybrid end effectors for soft robotic systems, there are major technical challenges associated with the assembly of a synthetic mimic using conventional fabrication methods.[16–19] In contrast to traditional prototyping approaches, multi-material 3D printing offers the potential for seamless fabrication of composite structures with complex architectures,[20] spanning a wide range of constituent moduli. In this study, we set out to fabricate a radially symmetrical end effector for hybrid robotics, inspired by the biological design principles already described. First, we performed a series of experimental and computational studies to investigate the shear and compression mechanical response of three conical tooth-like models (soft, rigid, and functionally graded) to identify the configuration that exhibited the capacity to apply highly focused point loads, while simultaneously minimizing structural damage. Informed by these results and deriving inspiration from the examples provided in Figure 1, we then used multi-material 3D printing to fabricate a pneumatically actuated, radially symmetrical hybrid end effector with six functionally graded tooth-like elements. Experimental testing was then carried out to quantify its puncturing capabilities, while simultaneously mitigating interfacial failure between the rigid and flexible phases.

Materials and Methods

Experiments

The conical tooth-like models and the hybrid end effector were designed by using SolidWorks, 3D computer-aided design software and printed with a multi-material 3D printer (Connex500; Stratasys Ltd.).

The shear and compression tests were performed on simplified conical tooth-like elements measuring 30 mm in height with a cone angle of 15°. The three models, that is, fully rigid, fully soft, and functionally graded (step-wise modulus gradient of nine different materials), were printed on a 10-mm-thick base of fully flexible material. To adapt the Instron testing machine for shear testing, custom sample holders were constructed to immobilize each conical test specimen. The tip of each conical sample was inserted into the conical profile hole in the substrate by adjusting the distance between the sample and the substrate by using a mechanical linear translation stage (60 mm Travel, X-Axis Rack & Pinion Stage; Edmund Optics) in the x-direction and the Instron stage controls in the y-direction. Locking the translation stage by using a setscrew secured the position of each sample during testing. Each sample was then sheared by displacing the substrate in the y-direction by using the Instron stage controls until failure was observed. For compression

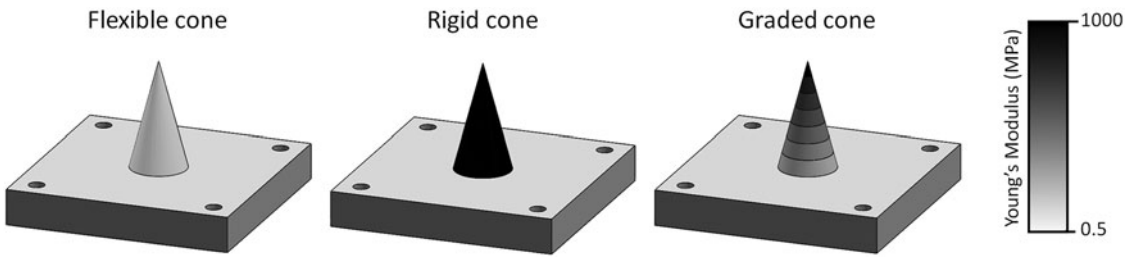

FIG. 2. Schematics of three different conical tooth-like models used in the study: soft, rigid, and functionally graded. The *gray* scale represents the range of elastic modulus of the materials in each model.

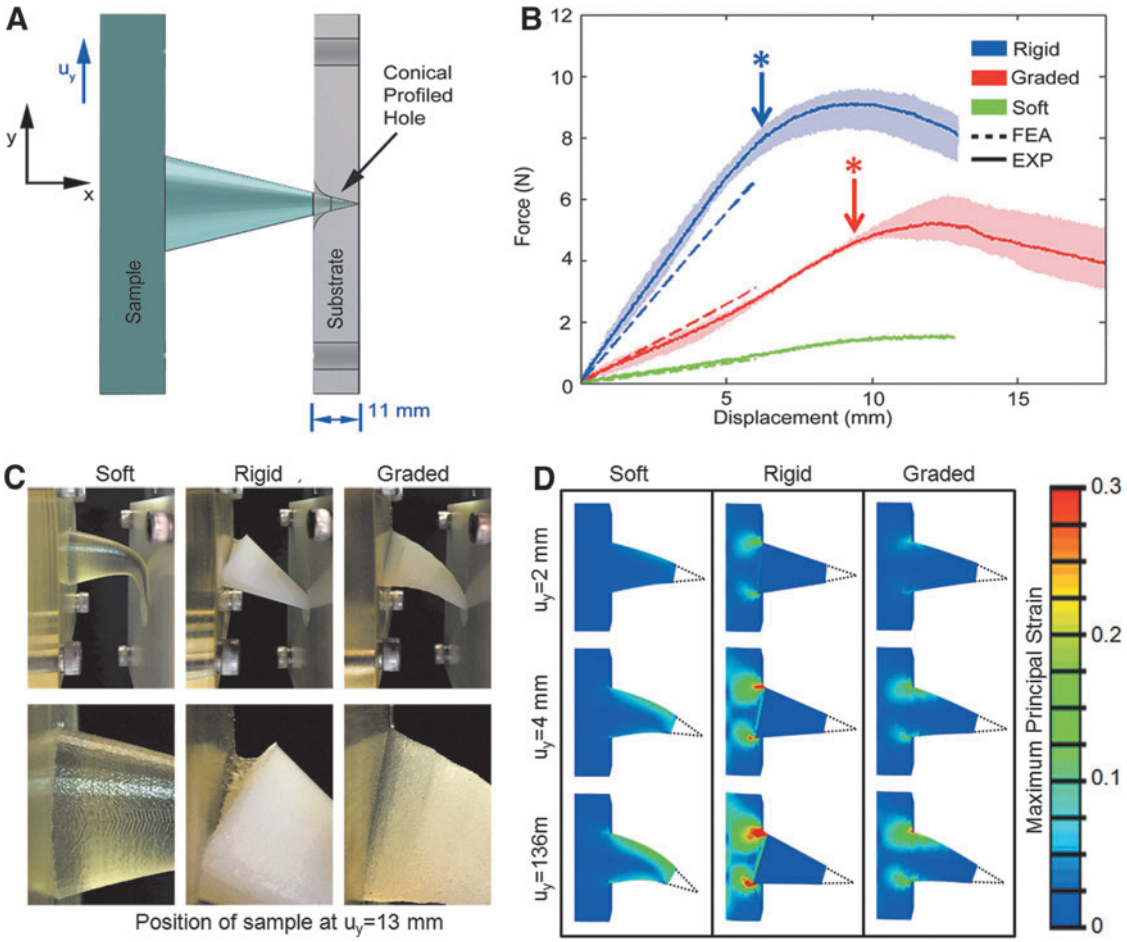

FIG. 3. Experimental and simulated shear tests of soft, rigid, and functionally graded conical tooth-like elements attached to a flexible base. We simultaneously measured the flexibility and anchoring of the three conical designs inside the punctured object under shear stress, while monitoring the integrity of the interface between the cone and its flexible substrate. **(A)** Schematic illustration of the shear testing rig. The conical sample was clamped 11 mm below the tip inside a 3D-printed conical profiled reference hole in the substrate and was displaced in the *y*-axis relative to the substrate. **(B)** Experimental (*solid lines*) and simulated (*dashed lines*) force displacement plots for the fully rigid, functionally graded, and soft conical configurations. The shaded region around each plot represents the standard deviation ($n = 4$) for each model. The *blue asterisk* indicates the point of interfacial failure in the rigid cone, and the *red asterisk* indicates the load at which the functionally graded cone displacement is transferred to the flexible base. **(C)** Photographs of the three conical models at displacement $u_y = 13$ mm (i.e., failure point for rigid and soft conical models) show the global cone deformation (*top images*) and the effect of shear force on the interface adjoining cones and the soft substrates (*bottom images*). The tip of the soft cone is dislodged from the reference hole and shows the worst anchoring stability inside the punctured reference object, whereas the rigid sample shows the maximum interfacial damage among the three conical models. **(D)** Simulated maximum principal strain distribution within the samples at shear displacements of $u_y = 2$, 4, and 6 mm.

Downloaded by Harvard University FRANCIS A COUNTWAY from online.liebertpub.com at 10/17/17. For personal use only.

testing, we reprinted the three different conical samples with the upper 5 mm of the tip removed to apply uniform compressive forces. Each sample was sandwiched between two compression plates, and stress was applied by displacing the top plate by 2.5 mm in the y-direction.

For pneumatic actuation of the hybrid end effector, a modified bicycle tire inner tube was cut and glued to adapt to the circular cavity surrounding the radially aligned tooth-like elements. An experimental test rig was constructed to measure the force applied by the tooth-like elements as a function of input pneumatic pressure. This rig consisted of six spring steel deflection beams that were used to simultaneously measure the force applied at the tip of each tooth-like element during a piercing act. To apply a compressive force on each tooth-like element, the end effector was pneumatically actuated at pressures ranging from 30 to 100 kPa. The forces were then calculated from the measured deflection of each beam based on their known material properties and geometries.

Simulations

To simulate the mechanical response of the fully rigid, fully soft, and functionally graded conical models under shear and compressive loading conditions and the hybrid end effector on actuation, non-linear finite element analysis was performed by using the commercial package Abaqus/Explicit (v6.12) (Abaqus Unified FEA; Dassault Systèmes). All materials were modeled by using a Neo-Hookean material model, each with a specific initial experimentally determined shear modulus.

Results

To investigate the mechanical benefits of a functionally graded tooth-like element under a shear loading and substrate penetration regime, we performed a series of tests on our three conical models (Fig. 2), which consisted of identical geometries (30 mm high; 15° cone angle) and a soft base (Young's modulus E = ca. 0.5 MPa), but with different material properties: soft (E = ca. 0.5 MPa), stiff (E = ca. 1.0 GPa), or one with graded Young's moduli (E ranging from ca. 0.5 MPa to ca. 1 GPa in 9 discrete steps[20]) by applying displacement (u_y) perpendicular to the longitudinal axis of the model by using a custom-designed sample holder (Fig. 3A). These studies revealed that among the three conical models, the soft cone (with the lowest stiffness of 0.13 N/mm) required the least amount of force per unit displacement (u_y = 12.84 mm), to become dislodged from the reference hole (Fig. 3B–C). In contrast, the rigid cone exhibited the maximum visible deformation at the point of contact between the cone and its base, and it failed at this interface at a similar displacement (u_y = 12.91 mm, Fig. 3C, lower images). By comparison, the functionally graded cone exhibited a behavior between that of

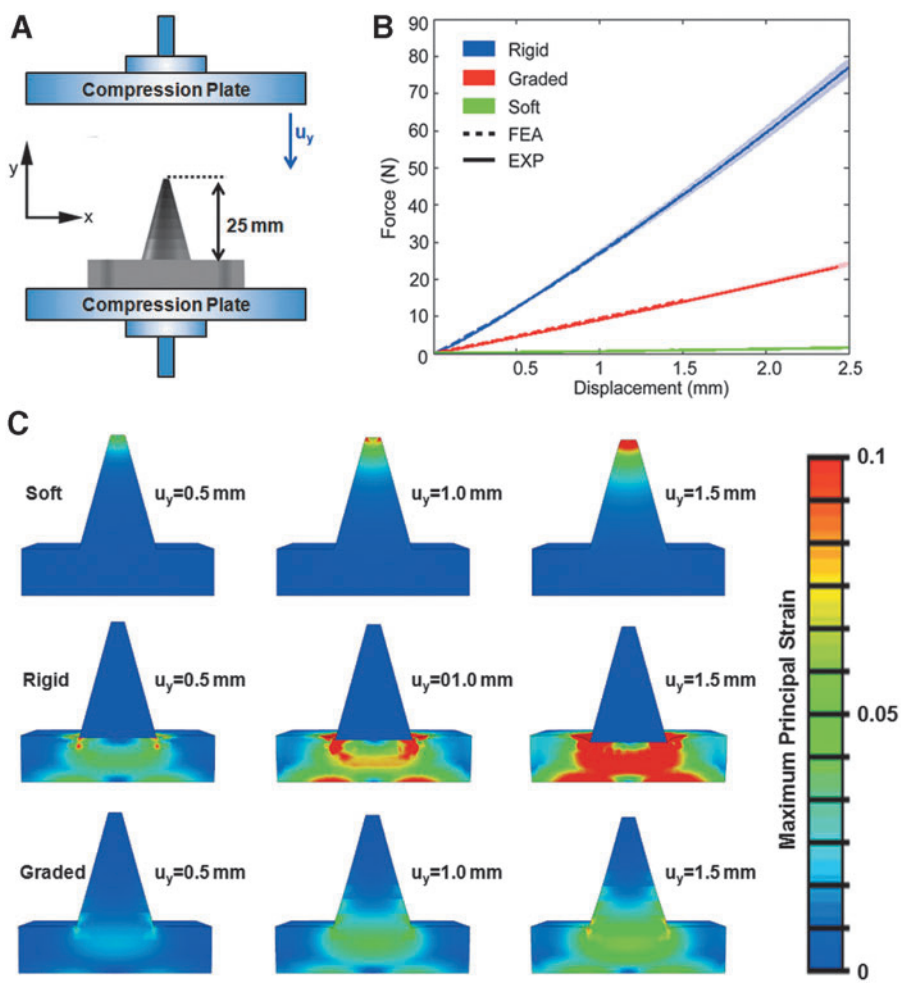

FIG. 4. Experimental and simulated compression tests of soft, rigid, and functionally graded conical tooth-like elements attached to a flexible base. **(A)** Schematic illustration of the compression testing rig. The conical sample, truncated at 5 mm below the tip, was compressed between two parallel plates by applying displacement u_y along the y-axis. **(B)** Experimental (*solid lines*) and simulated (*dashed lines*) compression response of fully rigid, graded, and soft conical models. The shaded region around each plot represents the standard deviation (n = 4) for each model. **(C)** Simulated maximum principal strain distribution within the samples at displacements of u_y = 0.5, 1.0, and 1.5 mm.

Downloaded by Harvard University FRANCIS A COUNTWAY from online.liebertpub.com at 10/17/17. For personal use only.

Downloaded by Harvard University FRANCIS A COUNTWAY from online.liebertpub.com at 10/17/17. For personal use only.

the fully flexible and fully rigid samples and demonstrated excellent ability to remain anchored inside the reference hole under shear loading. The modulus gradient from the flexible base to the rigid tip simultaneously increased the bending stiffness of the composite cone, while eliminating stress concentration and the onset of failure at the cone-base interface.

To validate our experimental results, we first estimated the axial strain in all three conical tooth-like models by using the linear elastic beam theory. The calculations show significant reduction in the maximum axial strain in a graded cone compared with fully rigid and soft conical models under both shear and compressive loading conditions. Importantly, the strain reduction in the graded cone occurs at the cost of only a moderate stiffness decline compared with the fully rigid cone model (see Supplementary Section S1 for details; Supplementary Data are available online at www.liebertpub.com/soro). Further, to capture both the effect of the substrate and that of the large deformations involved in the experimental tests, we conducted non-linear finite element simulations by using the commercial package Abaqus/Standard. The 3D models of the cones and the substrate were constructed by using second-order 3D continuum-reduced integration brick elements (Abaqus element type C3D20R). The mesh was most dense around the tip and coarsened toward the substrate, leading to $\sim$5000 elements for each model. Finally, the material responses were captured by using a nearly incompressible Neo-Hookean model with the experimentally measured Young's moduli.

The numerical shear results were generated by clamping the cone 11 mm below the tip and applying the displacement perpendicular to the length of the cone (in all of the simulations, the bottom surface of the substrate was completely fixed), in a manner similar to the experimental setup shown in Figure 3A. The analysis revealed good correspondence between experimental (solid lines) and simulated mechanical responses (dotted lines) for displacements ranging from $u_y = 0$ to 6 mm (Fig. 3B). Snapshots of the simulated maximum principal strain distributions within the three cone models at displacements of $u_y = 2$, 4, and 6 mm (Fig. 3D) further support the experimental results. Clearly, the maximum principal strain at any displacement is highest in the rigid cone model (2.5- and 1.7-fold at $x = 6$ mm, in comparison with soft and functionally graded designs, respectively), and it is concentrated at the cone-base interface. In contrast, the strain is uniformly distributed in the soft cone from the tip to the base, providing high flexibility, but at the cost of the ability to remain anchored inside the punctured reference object. The functionally graded design, however, facilitates strain diffusion at the cone-base interface, maintains low strain at the tip, while

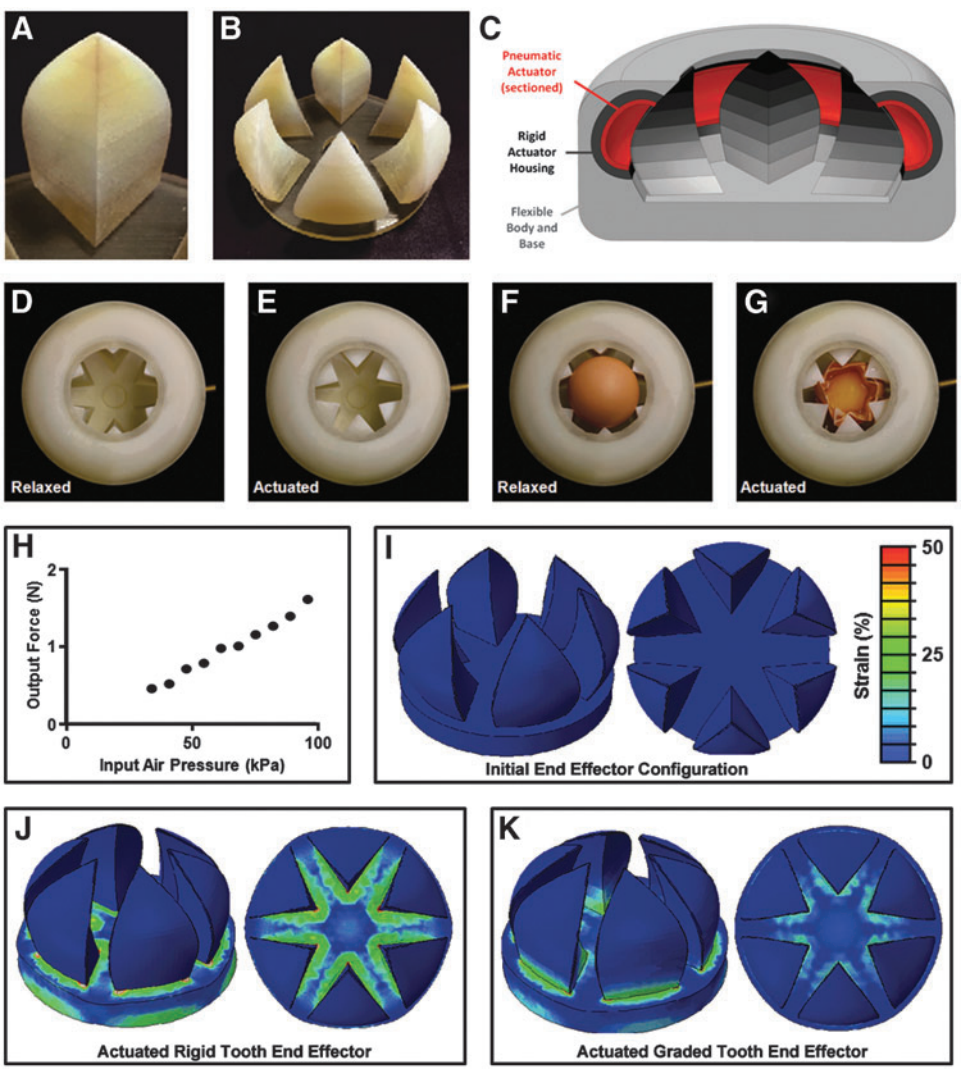

FIG. 5. Hybrid end effector assembly and mechanical characterization. **(A–C)** End effector architecture consisting of six radially arranged functionally graded tooth-like elements surrounded by an embedded pneumatic actuator. **(D–G)** Actuation of the end effector in the absence **(D–E)** and presence **(F–G)** of an egg to demonstrate the symmetrical application of an applied load. **(H)** Representative data of the measured output force as a function of the input air pressure to the end effector, revealing a maximum bite force of ca.1.7 N per tooth-like element. **(I–K)** Numerical results: Strain distribution in an end effector in the initial, undeformed configuration **(I)**, and during simulated pneumatic actuation of rigid **(J)** and functionally graded **(K)** tooth-like elements attached to a flexible basal plate.

Downloaded by Harvard University FRANCIS A COUNTWAY from online.liebertpub.com at 10/17/17. For personal use only.

sacrificing only a small amount of the flexibility inherent in the entire soft design, and exhibits an excellent ability to remain anchored inside the punctured reference object.

We also performed a series of compression tests on each conical model to simulate object penetration by the hybrid appendage. We used a truncated geometry for each of the three models by removing the upper 5 mm from the cone tips to apply uniform compressive forces and to avoid the sharp tips that almost immediately break at high stresses. The modulus gradient in the truncated cone was identical to the sharp-tip cone in shear experiments, and this contained only eight modulus steps and terminated with a material of $E = 0.9$ GPa at the truncated edge. Each sample was sandwiched between two compression plates, and deformation was applied by displacing the top plate to $u_y = 2.5$ mm (Fig. 4A). The experimental response recorded for each model ($n = 4$) showed a small deviation and revealed three curves that showed an almost linear relationship between force and displacement, with the slope defining the stiffness of the samples (Fig. 4A). As expected, the rigid cone exhibited the highest stiffness, whereas stiffness of the soft cone was one fiftieth of that exhibited by the rigid design, and thus, it lacked the rigidity necessary to effectively apply point loads to an object of interest. Compared with rigid and soft cones, the functionally graded design exhibited a moderate stiffness, which was approximately one third that of the rigid design.

The mechanical response predicted by numerical results for displacements ranging from $u_y = 0$ to 1.5 mm revealed good correspondence between experimental (solid lines) and simulated mechanical responses (dotted lines) (Fig. 4B). The numerical contour map of the principal strain at compressive displacements of $u_y = 0.5$, 1.0, and 1.5 mm further justifies the comparative mechanical response of the three conical models (Fig. 4C). Although the applied strain was not transferred to the cone-base interface in the soft design, the high concentrated strain of 40% at $u_y = 1.5$ mm around the tip led to large localized tip deformations. In contrast, the strain was localized around the cone-base interface in the rigid design, with a maximum value of 40% at the same displacement, suggesting permanent deformation at this interface during compression. In the functionally graded design, however, the strain was more evenly distributed, with a maximum local principal strain at displacement, $u_y = 1.5$ mm (11%), which was significantly lower than that observed for the other two material distributions, demonstrating increased failure resistance, while maintaining moderate stiffness.

These combined results demonstrate that in comparison to the completely soft or completely rigid designs, the functionally graded model offers maximum anchoring stability inside a punctured reference object by optimizing the bending stiffness and effectively reducing interfacial stresses on a soft substrate under both shear and compressive loading regimes. Based on these observations, and deriving inspiration from the examples provided in Figure 1, we used multimaterial 3D printing to fabricate a pneumatically actuated, radially symmetrical hybrid end effector with six functionally graded tooth-like elements (Fig. 5A) that interface with a flexible base (Fig. 5B, C). The shape of each tooth-like element was modified into a ''curved-wedge'' to provide a large contact area between the outer surface of tooth-like elements and the actuator, while maintaining a low bending stiffness. The wedge-like design also maximized the space between the opposing tooth-like elements to accommodate target objects of interest. The entire end effector geometry (excluding the pneumatic tube) was fabricated as a unitary piece in a single 3D print, thus achieving excellent interfacial adhesion between the constituent phases.[20] The actuation force was provided by a pneumatic tube that ran around the outside perimeter, between the tooth-like elements and the end effector body (Fig. 5C). When inflated, the relaxed pneumatic tube (Fig. 5D) expanded within a rigid circular cavity and applied a radially inward compressive force to actuate the inward bending of the tooth-like elements and, hence, facilitated nearly symmetrical puncturing of an object of interest (Fig. 5E).

Using an egg as a test subject placed in the center of the functionally graded end effector, we demonstrated its ability to apply uniform and highly localized stresses (Fig. 5F and Supplementary Video S1), which resulted in complete fracture of the egg (Fig. 5G) (the separated fractured circular cap of the egg shell was removed for photographic clarity after the test). To quantify the end effector's performance, we constructed a test rig to measure the output force applied at the tip of each tooth-like element as a function of input air pressure to the pneumatic actuator (see Supplementary Section S2 for details). The test rig consisted of six pre-calibrated spring steel deflection beams that were used to simultaneously measure the force applied at the tip of each tooth-like element during a loading event. After inflation of the pneumatic actuator to a specific air pressure, the deflection of each of the beams was measured to calculate the force applied by each tooth-like element (Fig. 5H). At a maximum applied pressure of 15 psi, we measured a bite force per tooth-like element of ca. 1.7 N.

Finally, to better understand the mechanical deformation modes of the end effector and the benefits of our biologically inspired design, we also performed non-linear static finite element simulations that incorporated either fully rigid or functionally graded tooth-like elements. We first constructed a 3D model of the end effector (Fig. 5I) and then imposed a uniform pressure to the outer surfaces of the six tooth-like elements to simulate their actuation. The simulations suggest that for the same deformation, a higher actuation pressure of 25 kPa would be required to bend the six rigid tooth-like elements compared with 14 kPa for their functionally graded counterparts. Moreover, the strain maps for the end effector with fully rigid tooth-like elements showed much larger strains on actuation (Fig. 5J) than for the functionally graded design (Fig. 5K). In both cases, the maximum strain was located at the interface adjoining each tooth-like element and the flexible base. However, in the case of functionally graded end effectors, the strain was diffused through each tooth-like element, thus reducing the maximum localized strain at the interface. Therefore, the advantages imparted to an end effector with a compositionally graded architecture are twofold. First, it offers effective puncturing at low actuation pressure, and second, it minimizes the structural damage by reducing both the global and local maximum strain at the interface adjoining the tooth-like elements and its flexible basal plate.

Conclusion

The present research illustrates the advantages of hybrid end effectors for soft robotic systems that demonstrate compliance and resilience owing to the presence of soft and highly

Downloaded by Harvard University FRANCIS A COUNTWAY from online.liebertpub.com at 10/17/17. For personal use only.

deformable actuators, while simultaneously possessing the ability to apply highly concentrated loads at their rigid termini and minimizing the onset of intrinsic structural damage. In addition, the fabrication of these hybrid end effectors via multi-material 3D printing provides significant advantages over conventional multi-component assembly-based approaches in that it facilitates the rapid design and construction of complex geometries while achieving excellent adhesion between the constituent phases. The hybrid architecture described here seamlessly integrates rigid and flexible components via a functionally graded interface, and thus, it shows great potential in the emerging field of soft robotics. Previous work has successfully demonstrated the value of soft robotics in the biomedical field,[21,22] and the incorporation of hybrid cutting and penetrating functionalities offers new possibilities for interacting with soft biological tissues during difficult interventional procedures. In addition to its value in robotics applications, the functionally graded design strategy described here could also be adapted for the flexible integration of electronic and electromechanical systems where the targeted functionality depends on the successful interfacing of rigid components to flexible thin film substrates.

Acknowledgments

This work was supported by funding from the Wyss Institute for Biologically Inspired Engineering and by the Materials Research Science and Engineering Center under the National Science Foundation Award (Grant No. DMR-1420570). K.B. and J.A. also acknowledge support from the National Science Foundation (Grant No. DMR-1533985). C.C. also acknowledges support from the National Science Foundation Graduate Research Fellowship under Grant No. DGE-1144086.

Authors' Contributions

J.C.W., M.T.T., J.A., D.E.I., and K.B. conceived the research; K.K., J.L., M.A., C.C., M.T.T., and J.C.W. performed the measurements. All authors analyzed the data and wrote the article. The authors thank Dorothy McLaren for the illustrations in Figure 1A and Shahrouz Amini and Ali Miserez (NTU) for the microCT data in Figure 1B.

Author Disclosure Statement

No competing financial interests exist.

References

1. Rus D, Tolley MT. Design, fabrication and control of soft robots. Nature 2015;521:467–475.
2. Trivedi D, Rahn CD, Kier WM, Walker ID. Soft robotics: biological inspiration, state of the art, and future research. Appl Bionics Biomech 2008;5:99–117.
3. Kim S, Laschi C, Trimmer B. Soft robotics: a bioinspired evolution in robotics. Trends Biotechnol 2013;31:287–294.
4. Majidi C. Soft robotics: a perspective—current trends and prospects for the future. Soft Robotics 2014;1:5–11.
5. Stokes AA, Shepherd RF, Morin SA, Ilievski F, Whitesides GM. A hybrid combining hard and soft robots. Soft Robotics 2013;1:70–74.
6. Pfeifer R, Lungarella M, Iida F. The challenges ahead for bio-inspired'soft'robotics. Commun ACM 2012;55:76–87.
7. Pfeifer R, Lungarella M, Iida F. Self-organization, embodiment, and biologically inspired robotics. Science 2007;318:1088–1093.
8. Suzumori K, Iikura S, Tanaka H. Applying a flexible microactuator to robotic mechanisms. IEEE Control Syst 1992;12:21–27.
9. Park Y, *et al.* Design and control of a bio-inspired soft wearable robotic device for ankle–foot rehabilitation. Bioinspir Biomim 2014;9:016007.
10. Polygerinos P, Wang Z, Galloway KC, Wood RJ, Walsh CJ. Soft robotic glove for combined assistance and at-home rehabilitation. Rob Auton Syst 2015;73:135–143.
11. Tolley MT, *et al.* A resilient, untethered soft robot. Soft Robotics 2014;1:213–223.
12. Dantzler WH. Comparative Physiology. New York: Oxford University Press, 1997.
13. Lichtenegger HC, *et al.* Zinc and mechanical prowess in the jaws of Nereis, a marine worm. Proc Natl Acad Sci U S A 2003;100:9144–9149.
14. Waite JH, Lichtenegger HC, Stucky GD, Hansma P. Exploring molecular and mechanical gradients in structural bioscaffolds. Biochemistry (New York) 2004;43:7653.
15. Miserez A, *et al.* Nanostructured materials: microstructural and biochemical characterization of the nanoporous sucker rings from *Dosidicus gigas*. Adv Mater 2009;21:n/a.
16. Ilievski F, Mazzeo AD, Shepherd RF, Chen X, Whitesides GM. Soft robotics for chemists. Angew Chem Int Ed Engl 2011;50:1890–1895.
17. Cho K, *et al.* Review of manufacturing processes for soft biomimetic robots. Int J Precis Eng Manuf 2009;10:171–181.
18. Lipson H. Challenges and opportunities for design, simulation, and fabrication of soft robots. Soft Robotics 2013;1:21–27.
19. Naleway SE, Porter MM, Mckittrick J, Meyers MA. Structural design elements in biological materials: application to bioinspiration. Adv Mater 2015;27:5455–5476.
20. Bartlett NW, *et al.* SOFT ROBOTICS. A 3D-printed, functionally graded soft robot powered by combustion. Science (New York) 2015;349:161.
21. Cianchetti M, Laschi C. Pleasant to the touch: by emulating nature, scientists hope to find innovative new uses for soft robotics in health-care technology. IEEE Pulse 2016;7:34–37.
22. Cianchetti M, Menciassi A. Soft robots in surgery. (Proceedings of the Soft Robotics Week, April 25–30, 2016). Soft Robotics: Trends, Applications and Challenges. Laschi C, Rossiter J, Iida F, Cianchetti M, Margheri L. (Eds). Livorno, Italy: Springer, 2017, pp. 75–85.

Address correspondence to:
James C. Weaver
Wyss Institute for Biologically Inspired Engineering
Harvard University
Boston, MA 02115

E-mail: james.weaver@wyss.harvard.edu

Katia Bertoldi
Harvard John A. Paulson School
of Engineering and Applied Sciences
Harvard University
Cambridge, MA 02138

E-mail: bertoldi@seas.harvard.edu

Supplementary Data

S1. Modeling of a Conical Tooth-Like Geometry Using the Linear Elastic Beam Theory

Here, we use the linear elastic beam theory to estimate the approximate stiffness and normal stress/strain components in a tooth-like conical geometry under both compression and shear. For these calculations, we consider a truncated cone model (Supplementary Fig. S1) with diameter $d(x) = d_l + (d_h - d_l)x/L$, where $d_h = 16$ mm is the base diameter, $d_l = 2.74$ mm is the tip diameter, and $L = 24.88$ mm is the height of the cone. Moreover, we assume the cone to be fixed at the base and to be made of linearly elastic materials.

Uniaxial compression

When a compressive force, F, is applied to the tip of the conical model, the external work, W_{ext}, is given by:

$$W_{ext} = \frac{1}{2} F\Delta, \tag{1}$$

where Δ is the resulting compressive displacement. Moreover, since under the framework of a one-dimensional linear elastic beam assumption, the axial stress $\sigma_x(x)$ and strain $\varepsilon_x(x)$ are considered uniform on each cross-section, the total strain energy, W_{int}, is

$$\begin{aligned} W_{int} &= \frac{1}{2}\int_0^L \sigma_x(x)\varepsilon_x(x)A(x)dx \\ &= \frac{1}{2}\int_0^L \frac{F}{A(x)}\frac{F}{E(x)A(x)}A(x)dx \\ &= \int_0^L \frac{2F^2}{E(x)\ \pi[d_l + (d_h - d_l)x/L]^2}dx \end{aligned} \tag{2}$$

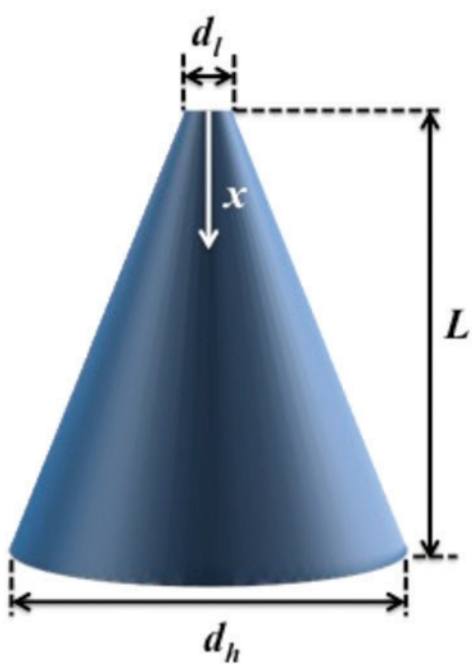

SUPPLEMENTARY FIG. S1. The geometry of tooth-like elements used in the analytical study.

where $A(x)$ is the area of cross-section, and $E(x)$ is Young's modulus at a point x along the length of the cone.

By equating Equations (1) and (2), the compressive displacement, Δ, can be expressed in terms of the applied force, F, as:

$$\Delta = \int_0^L \frac{4F}{E(x)\pi[d_l + (d_h - d_l)x/L]^2}dx, \tag{3}$$

so that the stiffness of the cone, K_c, and the axial strain, $\varepsilon_x(x)$, are given by

$$K_c = \frac{F}{\Delta} = \frac{1}{\int_0^L \frac{4}{E(x)\pi[d_l + (d_h - d_l)x/L]^2}dx}, \tag{4}$$

$$\begin{aligned} \varepsilon_x(x) &= \frac{F}{E(x)A(x)} \\ &= \frac{\Delta}{E(x)A(x)\int_0^L \frac{4}{E(x)\pi[d_l + (d_h - d_l)x/L]^2}dx}. \end{aligned}$$

To study the effect of Young's modulus on the stiffness and axial strain distribution of the truncated conical model under compressive loading, we compare three cases:

1. a uniform fully rigid cone with $E = 10$ MPa,
2. a uniform fully soft cone with $E = 1$ MPa,
3. a graded cone with a linearly varying E, $E(x) = 10\text{-}9x/L$.

Using Equation (4), we find that the stiffness for the soft, rigid, and graded conical structure is $K_c^s = 1.38$ N/mm, $K_c^r = 13.84$ N/mm, and $K_c^g = 9.27$ N/mm, respectively. On the other hand, by using Equation (5), the strains for the three cases are:

$$\begin{aligned} \varepsilon_x^s &= \frac{1.76\Delta}{(2.74 + 0.533x)^2}, \\ \varepsilon_x^r &= \frac{1.76\Delta}{(2.74 + 0.533x)^2}, \\ \varepsilon_x^g &= \frac{11.8\Delta}{(10 - 0.362x)(2.74 + 0.533x)^2}. \end{aligned}$$

Consequently, the maximum axial strain for both the rigid and soft cones ($\varepsilon_x^{max} = 0.2344\Delta$) is greater compared with that for the gradient cone ($\varepsilon_x^{max} = 0.1572\Delta$). Therefore, these simple analytical calculations demonstrate that the strain reduction in a graded cone occurs at the cost of only a moderate stiffness decline compared with the fully rigid model.

Shear

Similarly, when a shear force, F, is applied to the tip of the conical model, the external work, W_{ext}, is still given by

Equation (1), where Δ is the resulting shear displacement. The total strain energy, W_{int}, of the system under the framework of a one-dimensional linear elastic beam assumption is given by:

$$W_{int} = \frac{1}{2}\int_0^L \frac{[M(x)]^2}{E(x)I(x)}dx = \int_0^L \frac{32F^2x^2}{E(x)\,\pi[d_l + (d_h - d_l)x/L]^4}dx, \tag{6}$$

where $M(x) = Fx$ is the bending moment of the system, and $I(x) = \frac{\pi[d_l + (d_h - d_l)x/L]^4}{64}$ is the area moment of inertia.

By equating Equations (1) and (6), the shear displacement, Δ, can be determined as a function of the force F as

$$\Delta = \int_0^L \frac{64Fx^2}{E(x)\ \pi[d_l + (d_h - d_l)x/L]^4}dx, \tag{7}$$

so that the bending stiffness of the cone, K_s, and the axial strain, $\varepsilon_x(x)$, are given by

$$\mathrm{K_s} = \frac{\mathrm{F}}{\Delta} = \frac{1}{\int_0^L \frac{64x^2}{E(x)\ \pi[d_l + (d_h - d_l)x/L]^4}dx}, \tag{8}$$

$$\varepsilon_x(x) = \frac{\mathrm{M(x)d(x)}}{\mathrm{2E(x)I(x)}} = \frac{\mathrm{x}\Delta}{\mathrm{2E(x)}\pi[d_l + (d_h - d_l)x/L]^3 \int_0^L \frac{x^2}{E(x)\ \pi[d_l + (d_h - d_l)x/L]^4}dx}. \tag{9}$$

As for the case of uniaxial compression, we investigate the effect of Young's modulus on the bending stiffness and axial strain distribution. Using Equation (8), we find that the bending stiffness for the soft, rigid, and graded conical structure is $K_s^s = 0.11$ N/mm, $K_s^r = 1.1$ N/mm, and $K_s^g = 0.50$ N/mm, respectively. On the other hand, by using Equation (9), the strains for the three cases are:

$$\varepsilon_x^s = \frac{1.0931x\Delta}{(2.74 + 0.533x)^3},$$
$$\varepsilon_x^r = \frac{1.0931x\Delta}{(2.74 + 0.533x)^3},$$
$$\varepsilon_x^g = \frac{5.1270x\Delta}{(10 - 0.362x)(2.74 + 0.533x)^3}.$$

Consequently, for the case of shear loading, the maximum axial strain for both the rigid and soft cones ($\varepsilon_x^{max} = 0.041\Delta$) is greater than that in the gradient cone, $\varepsilon_x^{max} = 0.031\Delta$. By comparing the bending stiffness already calculated, it is evident that the strain reduction in a graded cone is achieved at the cost of only a moderate stiffness decline compared with the fully rigid model.

S2. Measurement of Bite Force of the Fabricated End Effector

The custom test rig for measuring the output force at the tips of the tooth-like elements in the end effector as a function of input actuation pressure is shown in Supplementary Figure S2. A pressurized air source was used to inflate the end effector's actuation bladder (a modified bicycle tube) from 5 to 15 psi in 1-psi increments. The test rig consisted of a set of 66×9 mm deflection beams cut out of 0.5-mm-thick spring steel (one for each tooth) and that were inserted into the end effector during actuation. A piece of machined aluminum with setscrews held all six beams in place. During testing, the rig was mounted at a fixed height above the end effector and a ruler was positioned behind the pair of beams, which allowed us to measure the deflections. The beam deflection corresponding to each actuation pressure was obtained by analyzing the photographs with public domain image processing software (Image J). Before collecting deflection data at each actuation pressure, the pressure in the inner tube was allowed to return to the atmosphere and the base position was noted at 0 psi.

The deflection for each beam was estimated by dividing the total deflection of both beams by two, while allowing for variations in horizontal alignment. The bite force and applied

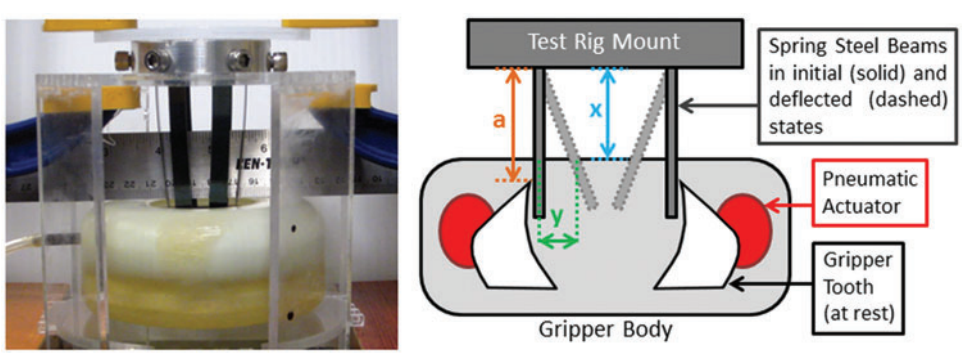

SUPPLEMENTARY FIG. S2. Photograph (*left*) and cross-section diagram (*right*) of experimental setup for bite force measurements. Photograph is of the deflected beams while pressure was applied to the inner tube inside the wall of the end effector. A pair of clamps secures the testing rig in place, and a ruler is positioned within the tooth-like elements of the end effector for determining the beam positions in each state. The accompanying schematic (*right*) shows the relative positions of the inner tube, tooth-like elements, and beams inside the end effector.

pressure of the end effector were calculated by using the following beam deflection equation derived from the Euler–Bernoulli beam theory:

$$F = \frac{6yEI}{(3x - a)x^2}$$

Here, y is the measured perpendicular deflection, E is the elastic modulus of the beam material, I is the beam's moment of inertia, x is the length of the beam at the point of measurement (at the bottom of the ruler), and a is the point of application, as shown in the diagram in Supplementary Figure S2 (right image). The elastic modulus of the beam material was experimentally measured by using an Instron compression tester by collecting the stress-strain data for each beam. Due to the motion of the tooth-like elements during actuation, we found the point of application to vary by ~ 1.8 mm between the 5 and 15 psi actuation cases. We approximated this variation by using a linear function for the value of a at intermediate pressures.

SUPPLEMENTARY VIDEO S1. The video shows the ability of the 3D-printed hybrid end effector to apply localized stress on an object of interest; for example, it can crush an egg by applying a highly localized force.